Chemical Papers (2023) 77:6655–6667
https://doi.org/10.1007/s11696-023-02966-2

ORIGINAL PAPER

Battery-type $NiMoO_4$@$NiMoS_4$ composite electrodes for high-performance supercapacitors

Xinrong Lv[1] · Xiaoqin Min[1] · Xiaoyun Lin[1] · Yongnian Ni[1]

Received: 11 May 2023 / Accepted: 7 July 2023 / Published online: 14 July 2023

Abstract

A novel $NiMoO_4$@$NiMoS_4$/NF nanocomposite is facilely grown on nickel foam (NF) *via* hydrothermal reaction and high-temperature calcination methods. The $NiMoO_4$@$NiMoS_4$/NF possesses a specific nanorods@nanosheets core–shell structure, greatly facilitating the transfer of electrons and ions. So, the $NiMoO_4$@$NiMoS_4$/NF shows excellent electrochemical performance. When a current density is 1 A g^{-1}, the specific capacity (C_p) of $NiMoO_4$@$NiMoS_4$/NF reaches 1996 C g^{-1}, which is 7 times that of single $NiMoO_4$/NF, and its C_p is higher than the C_p of other Ni-Mo-based electrode materials reported in the literatures. Moreover, the $NiMoO_4$@$NiMoS_4$/NF has a long cycling life, and its capacity retention rate reaches 83.1% after 5000 cycles at 20 A g^{-1}. The hybrid supercapacitor—$NiMoO_4$@$NiMoS_4$/NF-2//AC with $NiMoO_4$@$NiMoS_4$/NF as the positive electrode and AC as the negative electrode has an energy density of 32.75 Wh kg^{-1} and a power density of 725.09 W kg^{-1}. So the $NiMoO_4$@$NiMoS_4$/NF is a promising high-performance electrode material for battery-type hybrid supercapacitors.

Keywords $NiMoO_4$@$NiMoS_4$ nanocomposite · Core–shell structure · High-performance supercapacitors · Battery-type electrode materials

Introduction

With the rapid development of electric vehicles, portable electronic devices and other energy storage devices, the development of efficient, safe, renewable, clean and green energy storage devices has become the focus of attention (Li et al. 2018; Krishnamoorthy et al. 2018). Supercapacitors (SCs) possess high power and energy densities, long cycle life, environmental protection, flexibility and small size and have become an excellent candidate for energy storage (Zhai et al. 2020; Shao et al. 2015; Liu et al. 2017; Chen et al. 2020; Salunkhe 2016). On the basis of the energy storage principle, electrode materials for supercapacitors include electric double-layer capacitors (EDLCs) materials (Ji et al. 2014; Choi et al. 2012) and pseudocapacitors (PCs) materials (Banda et al. 2021; Boota et al. 2019) and battery-type capacitors (BTCs) materials (Zhaon et al. 2022; Wang et al. 2021). The positive and negative electrodes of EDLCs store energy by forming a double layer between the electrode surface and the electrolyte, which is mainly caused by the increase or decrease of high-energy conduction electrons on the electrode surface and does not produce an electrochemical reaction, and the energy storage process is reversible. In general, the electrode materials of EDLCs mainly include activated carbon (AC) (Kostoglou et al. 2018), carbon nanotubes (CNT) (Zhao et al. 2020) and graphene (Xu et al. 2015) and so on. Also, the most common electrode materials for PCs are conductive polymers (Cho et al. 2008) and transition metal compounds (Sathiya et al. 2011). However, PCs (BTCs) are caused by the underpotential deposition method, highly reversible chemical adsorption and desorption or redox reaction of the active electrode materials in the two-dimensional (2D) or quasi-2D space (Salunkhe et al. 2016), and its maximum charge–discharge capacity is controlled by the transfer rate of ions and charges on the surface of the electroactive materials, so charge transfer can be carried out in a short time, that is to say, higher specific power can be obtained. Therefore, PCs (BTCs) have a higher

Xinrong Lv and Xiaoqin Min have contributed equally.

✉ Xiaoyun Lin
linxiaoyun@ncu.edu.cn

[1] College of Chemistry and Chemical Engineering, Nanchang University, Nanchang 330031, China

specific capacity (C_p) and an energy density than EDLCs (Jayachandiran et al. 2021; Yang et al. 2020).

Transition metal oxides (TMOs), such as MnO_2 (Najafpour et al. 2015), V_2O_5 (Fleischmann et al. 2017), Co_3O_4 (Priyadharsini et al. 2020), RuO_2 (Ates et al. 2020), NiO (Ates et al. 2020), have been attracting increasing attention on account of their relatively high theoretical capacity, variable oxidation states, environmental protection and low cost. However, TMOs often have some disadvantages such as low mechanical stability and poor electrical conductivity. It is well known that transition metal sulfides (TMSs) such as MoS_2 (Savjani et al. 2016), Co_3S_4 (Shrivastav et al. 2020), NiS_2 (Azad et al. 2020) have a smaller band gap, better conductivity and better rate capability than TMOs. Bimetallic sulfides (BMSs) are widely used in energy storage devices such as lithium ion batteries (Lv et al. 2018; Guo et al. 2019), solar cells (Yu et al. 2020; Tang et al. 2020), sensors (Mariyappan et al. 2020) and SCs (Tao et al. 2018; Zhai et al. 2019) due to their diverse crystalline structure, higher conductivity and superior electrochemical activity compared with oxides. Molybdenum-based bimetallic sulfides have widely used in supercapacitors due to their high conductivity, accessibility, additional capacity of Faradic reaction in the center of Mo atom and multiple oxidation states from + 2 to + 6 (Xu et al. 2020). Meanwhile, nickel (Ni) is a common variable metal (Ni^{3+}/Ni^{2+}) and possesses a good magnetism and plasticity. Also, its chemical properties are relatively reactive, but more stable than iron, which is conducive to the redox reaction to improve the electrochemical energy storage performance. Mo-Ni-based bimetallic sulfides show a prospective electrochemical performance, which may be caused by a synergistic effect of Mo and Ni. The spongy $NiMoS_4$ synthesized by Xu et al. shows a C_p of 233 mAh g^{-1} at 0.75 A g^{-1} and a retention of 84% after 8000 cycles (Xu et al. 2020). The $NiMoS_4$-A synthesized by Du et al. shows a C_p of 313 C g^{-1} at 1 A g^{-1} and a retention rate of 82% after 10,000 cycles (Du et al. 2017). However, there is a certain gap between the reported C_p and theoretical C_p for $NiMoS_4$. Therefore, it is imperative to choose a suitable simple synthesis method and regulate a suitable structure to increase the C_s of $NiMoS_4$ (Shrestha et al. 2021). In this study, a novel $NiMoO_4$@$NiMoS_4$/NF core–shell nanocomposite was obtained by an in situ growth method and a high-temperature calcination method. Due to the unique nanorods@nanosheets core–shell heterostructures, the electrode material possesses a more abundant electrochemical active surface area and sites, showing excellent electrochemical performance in capacitor storage. Additionally, the $NiMoO_4$@$NiMoS_4$ material is directly deposited on NF, which avoids the addition of binders during electrode construction, thus improving the conductivity, rate capability and C_p of the electrode materials.

The aims of this investigation are: (1) to characterize the $NiMoO_4$/NF and $NiMoO_4$@$NiMoS_4$/NF nanocomposite via X-ray diffraction (XRD), scanning electron microscope (SEM), transmission electron microscope (TEM) and X-ray photoelectron spectroscopy (XPS) techniques; (2) to study the electrochemical performance of $NiMoO_4$/NF and $NiMoO_4$@$NiMoS_4$/NF with the use of cyclic voltammetry (CV), electrochemical impedance spectroscopy (EIS) and galvanostatic charge–discharge (GCD); and (3) to investigate the electrochemical performance of hybrid supercapacitor based on $NiMoO_4$@$NiMoS_4$/NF and activated carbon (AC).

Experimental

Chemicals

$NaMoO_4$ $2H_2O$ (100 g, 99.95%), potassium hydroxide (KOH), $(NH_4)_2S$, $Ni(NO_3)_2$ $6H_2O$, other chemicals (analytical reagent) were purchased from Xilong Chemical Co., Ltd. (Guangdong, China).

Pretreatment of NF

The NF was cut to the size of 1×1 cm^2 and then, respectively, placed in hydrochloric acid (3 M HCl), ethanol and ultra-pure water with ultrasonic for 10 min to remove surface oxides and impurities.

Preparation of $NiMoO_4$/NF

$Ni(NO_3)_2 \cdot 6H_2O$ (0.87 g) and $NaMoO_4 \cdot 2H_2O$ (0.73 g) were placed into a 200 mL of beaker, and 60 mL ultrapure water was added for stirring for 15 min continuously. Then the pretreated NF and the mixed solution were together transferred into a 100-mL reactor (Teflon-lined autoclave) and heated at 150 °C for 5 h. The NF loaded with materials was washed with ultra-pure water (UPW) and absolute alcohol several times in sequence and dried in vacuum at 80 °C for 12 h. Finally, the above sample ($NiMoO_4$/NF) was calcined in argon (Ar) at 300 °C in a tube furnace for 2 h.

Preparation of $NiMoO_4$@$NiMoS_4$/NF

The synthesized $NiMoO_4$/NF was vulcanized at 70 °C for 8 h in 60 mL $(NH_4)_2S$ solution with different concentrations (5, 10 and 15 mM) to obtain $NiMoO_4$@$NiMoS_4$/NF (marked as $NiMoO_4$@$NiMoS_4$/NF-1, $NiMoO_4$@$NiMoS_4$/NF-2 and $NiMoO_4$@$NiMoS_4$/NF-3, respectively). The obtained samples ($NiMoO_4$@$NiMoS_4$/NF) were cleaned with UPW and absolute alcohol several times in turn and dried in vacuum at 80 °C for 12 h. The active material attached to NF was

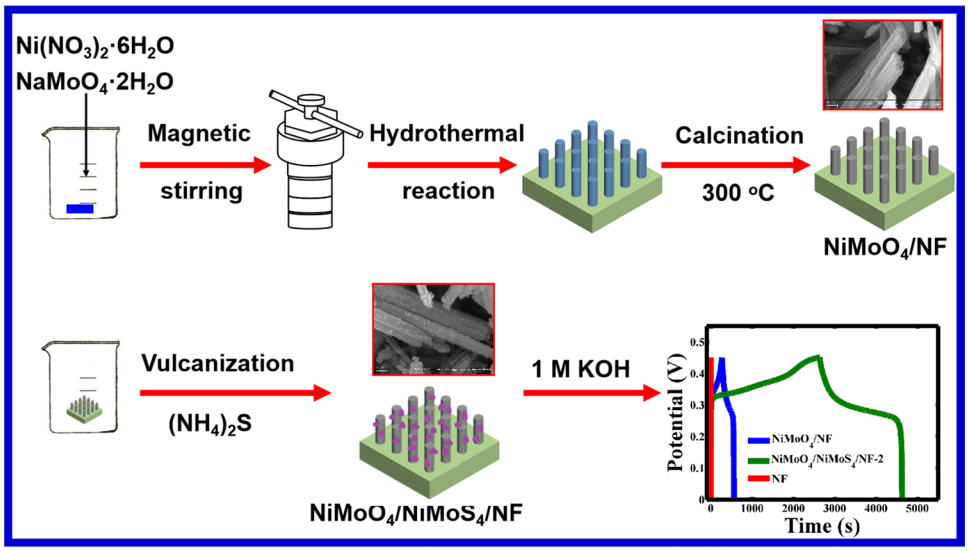

Scheme 1 The schematic diagram of the synthesis method for $NiMoO_4$@$NiMoS_4$/NF

approximately 1.0 mg. Scheme 1 is the schematic diagram of the synthesis method for $NiMoO_4$@$NiMoS_4$/NF.

Material characterizations

Crystal information, sample composition and morphology were obtained by XRD with the 2θ range from 5° to 80° (Bruker D8 Advance), XPS (Thermo Fisher, Nexsa), SEM (ZEISS MERLIN Compact) and TEM (Tecnai G2 F20).

Electrochemical measurement

Electrochemical methods including CV, EIS and GCD were performed on an electrochemical workstation (CHI660A, Shanghai Chenhua Co., LTD) in 1 M KOH electrolyte. Ag/AgCl, Pt wire and $NiMoS_4$@$NiMoO_4$/NF were used as the reference, auxiliary and working electrodes, respectively. In a two-electrode system, a $NiMoO_4$@$NiMoS_4$/NF-2//AC hybrid device was constructed through $NiMoO_4$@$NiMoS_4$/NF-2 as the positive electrode and AC as the negative electrode. The specific process is as follows: Acetylene black, polyvinylidene fluoride and AC were accurately weighed according to the mass ratio of 1:1:8 and transferred to an agate mortar. An appropriate amount of N-methyl-2-pyrrolidinone (NMP) was added and ground into a homogeneous paste. A certain amount of paste was coated on the NF and dried in vacuum for 12 h to obtain AC electrode. Both $NiMoO_4$@$NiMoS_4$/NF and AC electrodes should be immersed into 1 M NaOH electrolyte to activate for 12 h before use.

According to the charge balance theory of the asymmetric device (ASC) ($Q^+ = Q^-$), the charge stored in a capacitor depends on the C_p and active mass of the electrode. In this study, the active materials of $NiMoO_4$@$NiMoS_4$/NF and AC were 1 and 15 mg, respectively. That is, the mass ratio of positive electrode ($NiMoS_4$@$NiMoO_4$) and negative electrode (AC) is 0.067.

The specific capacitance (C_s, F g^{-1}), C_p (C g^{-1}), energy density (E) and power density (P) are calculated by the following formula (1–4) (D.W. Du et al. 2017).

$$C_s = I\Delta t/\Delta V \times m \tag{1}$$

$$C_p = I\Delta t/ \times m \tag{2}$$

$$E = (1000/2 \times 3600)C_p\left(\Delta V^2\right) \tag{3}$$

$$P = 3600E/\Delta t \tag{4}$$

Results and discussion

Characterization of $NiMoO_4$ and $NiMoO_4$@$NiMoS_4$

XRD was performed to study the crystal structure of the prepared $NiMoO_4$ and $NiMoO_4$@$NiMoS_4$. The XRD pattern of $NiMoO_4$ shows responses (Fig. 1A) at 2θ (degree) = 14.3, 18.9, 28.9, 32.8, 38.8, 43.9, 47.5 and 56.7° are attributed to the $NiMoO_4$ (110), (− 201), (220), (022), (112), (330), (− 204) and (024), respectively (JCPDS No. 86–0361) (M.J. Gao et al. 2019). Additionally, the patterns of $NiMoO_4$ are in good accordance with $NiMoO_4{\cdot}xH_2O$ (JCPDS No.13–0128), indicating the successful synthesis for the $NiMoO_4$ electrode material. However, it is difficult to determine the full crystal structure because the detail information of $NiMoO_4{\cdot}xH_2O$ is still not clear. The characteristic diffraction peaks of $NiMoO_4$@$NiMoS_4$ are consistent with the characteristic diffraction peak of $NiMoO_4$, showing that $NiMoS_4$ is a typical

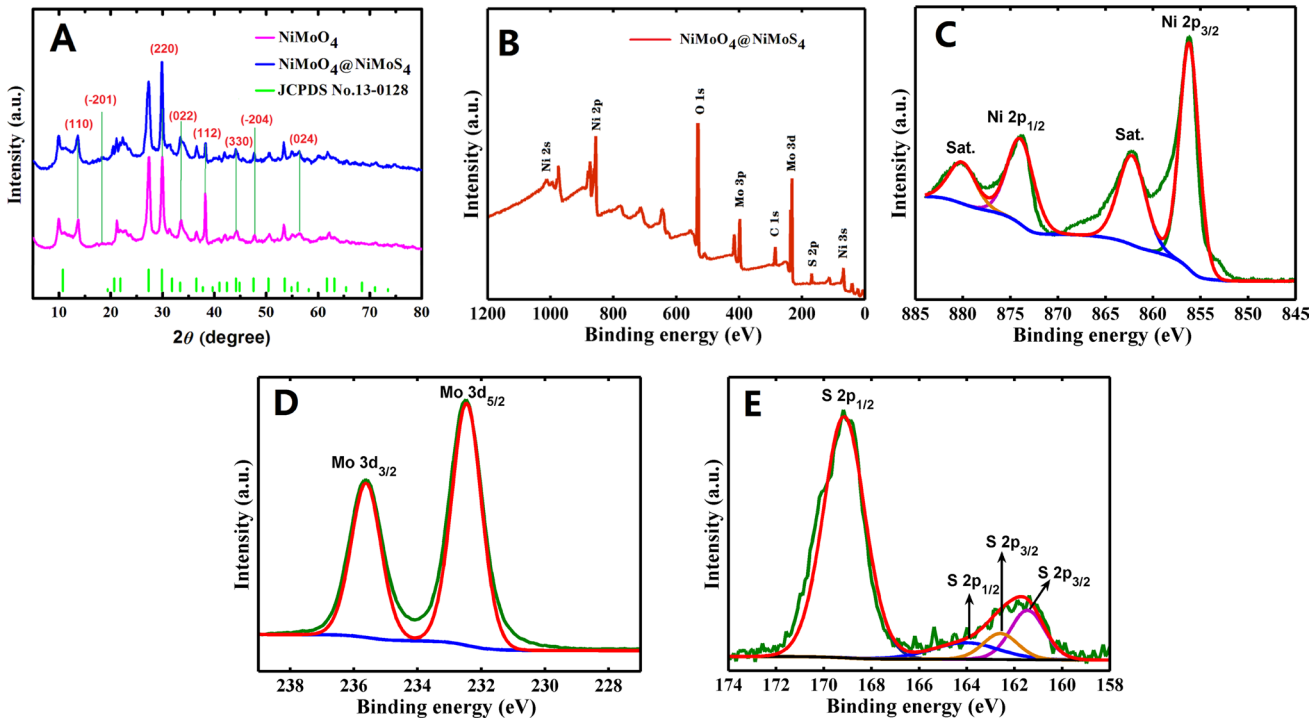

Fig. 1 **A** XRD patterns of $NiMoO_4$@$NiMoS_4$ and $NiMoO_4$; **B** XPS patterns of $NiMoO_4$@$NiMoS_4$; **C** Ni 2p, **D** Mo 3d and **E** S 2p of $NiMoO_4$@$NiMoS_4$

amorphous characteristic, so no other obvious characteristic peaks appear. Additionally, the some characteristic peaks of $NiMoO_4$@$NiMoS_4$ are weaker than that of $NiMoO_4$, which further proves that $NiMoS_4$ on the surface is a typical amorphous structure (Gao et al. 2019).

XPS is an important means of characterization of materials, and it can provide not only general chemical information, but also surface, microregion and depth distribution information of materials. Figure 1B indicates full scan spectrum of $NiMoS_4$@$NiMoO_4$ nanoparticles; Ni, Mo, S and O elements can be clearly observed in full scan spectrum. According to Fig. 1C, the Ni 2p spectrum is formed by fitting four distinct peaks. Peaks at 856.3 and 873.8 eV correspond to Ni $2p_{3/2}$ and Ni $2p_{1/2}$, respectively, while the peaks at 862.2 and 880.1 eV correspond to their satellite peaks, respectively, which are in line with Ni^{2+}. From Fig. 1D, two obvious peaks at 232.5 and 235.6 eV correspond to Mo $3d_{5/2}$ and Mo $3d_{3/2}$, and their dissociative binding energy is 3.1 eV, which conforms to Mo^{6+}. In Fig. 1E, the binding energies at 161.8 and 169.2 eV correspond to S $2p_{3/2}$ and S $2p_{1/2}$, respectively, indicating that the valence of S in the $NiMoS_4$ sample is −2 (Xu et al. 2020).

Figure 2 shows SEM images of the $NiMoO_4$ and $NiMoO_4$@$NiMoS_4$ samples. From Figs. 2A-2F, rod and columnar nanostructured materials are observed with approximately 35–50 nm in diameter and 0.1–0.3 μm in length, some of the powder agglomerating. The biggest difference between $NiMoO_4$ (Figs. 2A-2C) and $NiMoO_4$@$NiMoS_4$ (Figs. 2A-2E) is the surface structure of two kinds of materials. It is completely obvious that the surface morphology of $NiMoO_4$ is relatively smooth, and that of $NiMoO_4$@$NiMoS_4$ is rough and uneven, and a large number of nanosheets attach to the surfaces of cylinders to form a core–shell structure.

Figure 3 is the color mapping of oxygen (O), nickel (Ni), molybdenum (Mo) and sulfur (S) elements (B, C, D and E) of $NiMoO_4$@$NiMoS_4$. It is very apparent that the O, Ni, Mo and S elements were detected in the $NiMoO_4$@$NiMoS_4$ nanocomposite, indicating that partial O element in the $NiMoO_4$@$NiMoS_4$ composite was indeed replaced by the S element, which further demonstrates the successful synthesis for the $NiMoO_4$@$NiMoS_4$ nanocomposite. According to Fig. 3B, a large number of O elements exist in $NiMoO_4$@$NiMoS_4$, due to the fact that the $NiMoO_4$ mainly exists in the core part of $NiMoO_4$@$NiMoS_4$. From Fig. 3C, only some sparse dots are observed, but this does not mean the lack of Ni element in $NiMoO_4$@$NiMoS_4$ composite, which can be interpreted that the Ni element mainly exists in the inner "core," and it is less distributed in the outer "shell" of materials (Shrestha et al. 2021).

The detailed morphology and microstructure of prepared materials were further investigated by TEM, and the $NiMoO_4$ and $NiMoO_4$@$NiMoS_4$ samples were obtained through an ultrasonic stripping method, respectively. TEM

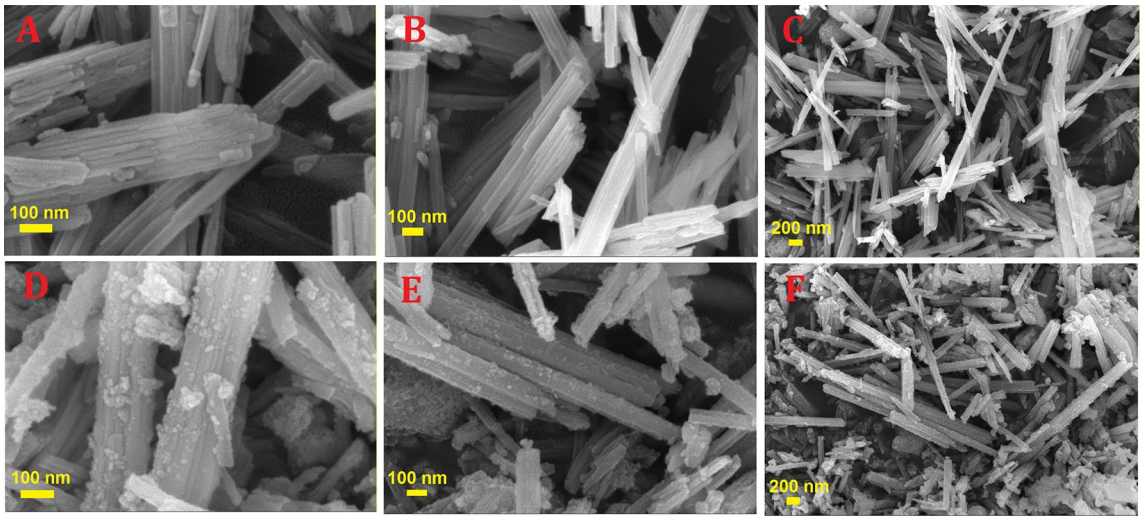

Fig. 2 SEM images of $NiMoO_4$ (**A**, **B** and **C**) and $NiMoO_4$@$NiMoS_4$ (**D**, **E** and **F**)

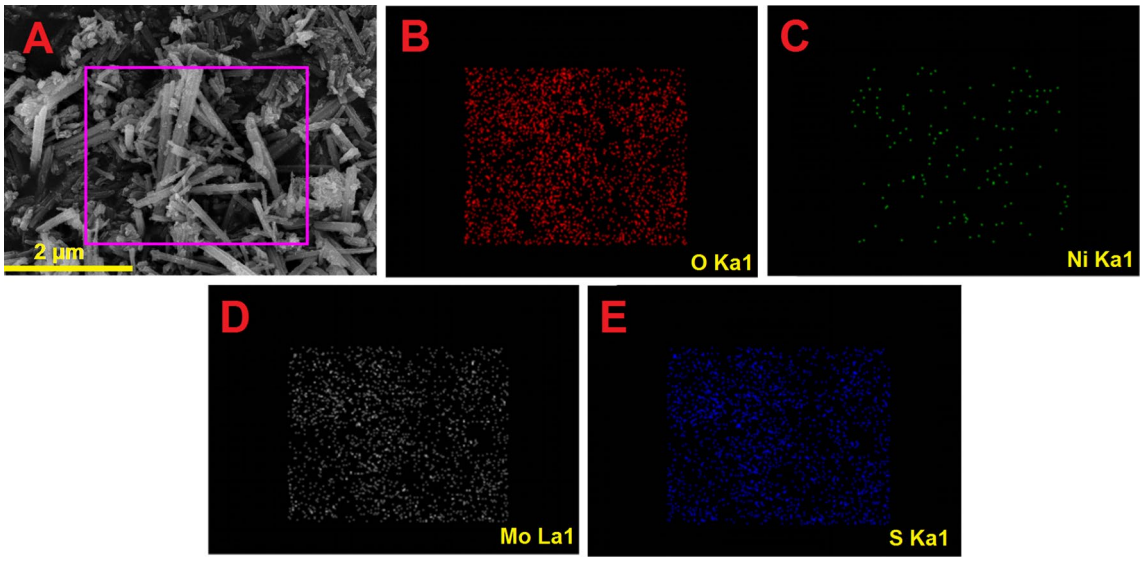

Fig. 3 SEM image of the $NiMoO_4$@$NiMoS_4$ (**A**); the corresponding elemental mapping of $NiMoO_4$@$NiMoS_4$ of O, Ni, Mo and S (**B**, **C**, **D** and **E**)

images of the $NiMoO_4$ and $NiMoO_4$@$NiMoS_4$ samples are shown in Figs. 4(A and B) and Figs. 4 (D and E). A rod-like nanostructure was observed in $NiMoO_4$ and $NiMoO_4$@$NiMoS_4$ samples. However, compared with $NiMoO_4$ (Fig. 4(A and B)), the $NiMoO_4$@$NiMoS_4$ (Fig. 4(D and E)) has an core–shell structure, and such core–shell structure makes $NiMoO_4$@$NiMoS_4$ nanocomposite have a lot of active surface, reduce the dead volume, promote the rapid redox process, generate rich induced current and improve the stability of electrochemical cycle. Additionally, the high-magnification TEM (HRTEM) images for the $NiMoO_4$ and $NiMoO_4$@$NiMoS_4$ samples are shown in Figs. 4 (C and F). From Fig. 4C, the lattice fringes of $NiMoO_4$ sample were observed distinctly, and the lattice spacings were measured to be 0.621 and 0.228 nm, which correspond to (110) and (112) lattice planes of $NiMoO_4$. Figure 4F shows the HRTEM image of $NiMoO_4$@$NiMoS_4$, and the lattice spacings of 0.621 and 0.228 nm were also observed, corresponding to (110) and (112) lattice planes of $NiMoO_4$, which further confirms that the "core" part of the material is made up of $NiMoO_4$.

In order to clearly distinguish the differences in material properties before and after vulcanization, the specific surface area and pore size distribution of the $NiMoO_4$/NF and $NiMoO_4$@$NiMoS_4$/NF-2 electrode materials were examined. The adsorption isotherms of the two electrode

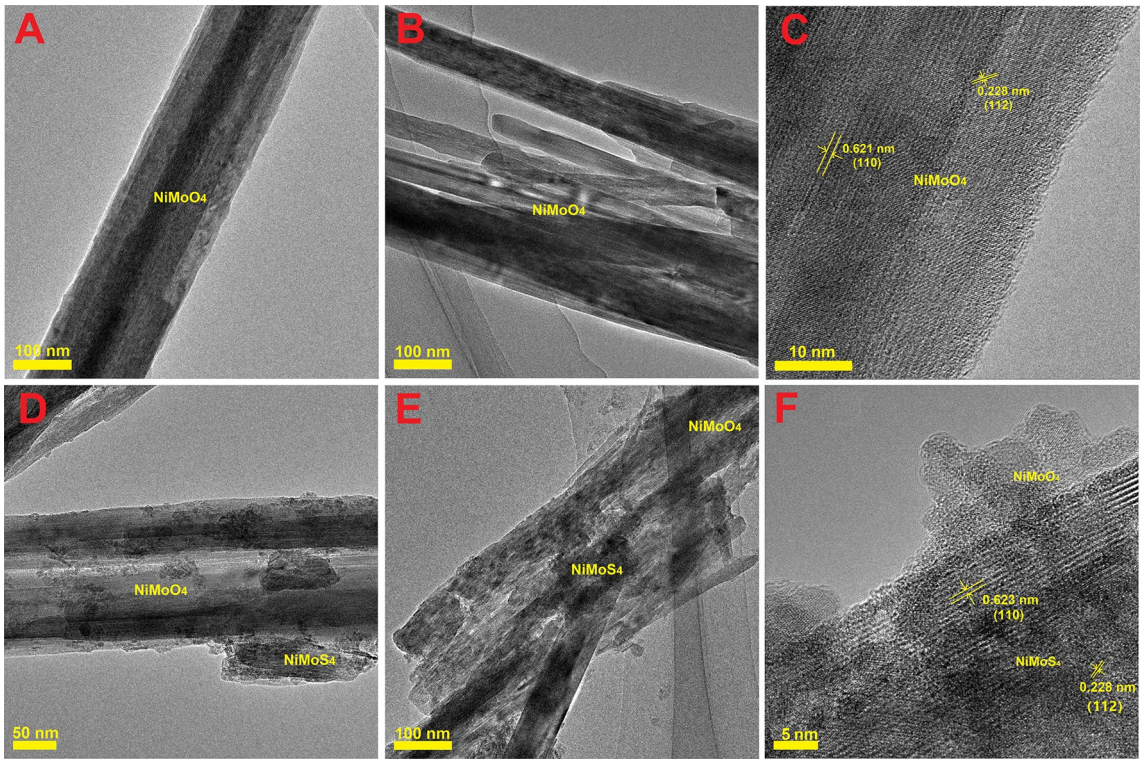

Fig. 4 TEM and HRTEM images of $NiMoO_4$ (**A**, **B** and **C**) and $NiMoO_4$@$NiMoS_4$ (**D**, **E** and **F**)

materials are shown in Figs. 5A and 5B. Typical isotherm type IV was presented according to the IUPAC classification. Based on BET-specific surface area measurements and the BJH method, the $NiMoO_4$@$NiMoS_4$/NF-2 (20.488 m^2/g) had a larger BET surface area than the $NiMoO_4$ (18.128 m^2/g). The pore size distributions (PSD) of the $NiMoO_4$/NF and $NiMoO_4$@$NiMoS_4$/NF-2 electrodes are shown in Figs. 5C and 5D. The average pore sizes of $NiMoO_4$/NF and $NiMoO_4$@$NiMoS_4$/NF-2 were calculated to be ~ 17.377 and ~ 14.414 nm through BJH method, respectively, which supports the observation as the majority of the pores lie in the mesoporous region in all of the specimens.

Electrochemical performance of $NiMoO_4$/NF and $NiMoO_4$@$NiMoS_4$/NF-2

In a three-electrode system, the electrochemical tests of $NiMoO_4$/NF and $NiMoO_4$@$NiMoS_4$/NF-2 were carried out by CV, EIS and GCD measurements in 1 M KOH solution. Figure 6A is the CV curves of $NiMoO_4$@$NiMoS_4$/NF-2, $NiMoO_4$/NF and NF within a voltage window of 0–0.6 V at 5 mV s^{-1}. A pair of redox peaks are observed, showing that the redox reaction is a quasi-reversible process, which demonstrates the battery-type characteristics for the $NiMoO_4$/NF and $NiMoO_4$@$NiMoS_4$ /NF-2 electrode materials. In general, the integral area enclosed by CV curve corresponds to the C_p value of the electrode material. From Fig. 6A, the electrochemical signal for the NF is negligible compared with the $NiMoO_4$/NF and $NiMoO_4$@$NiMoS_4$/NF-2. So the capacity contribution of the $NiMoO_4$/NF and $NiMoO_4$@$NiMoS_4$/NF-2 mainly originates from the active material themselves (Xu et al. 2020). The area of $NiMoO_4$@$NiMoS_4$/NF-2 is much larger than that of $NiMoO_4$/NF, indicating that $NiMoO_4$@$NiMoS_4$/NF-2 electrode material has relatively excellent electrochemical performance and can generate the maximum specific capacity. The capacity of $NiMoO_4$/NF and $NiMoO_4$@$NiMoS_4$/NF-2 is mainly contributed by the Faraday redox reaction of Ni^{2+}/Ni^{3+} (Eqs. (6 and 7) (Gao et al. 2019).

$$Ni^{2+} + 2OH^- = Ni(OH)_2 \quad (5)$$

$$Ni(OH)_2 + OH^- = NiOOH + H_2O + e^- \quad (6)$$

Figure 6B is the GCDs of $NiMoO_4$@$NiMoS_4$/NF-2, $NiMoO_4$/NF and NF within a voltage window of 0–0.45 V at a current density of 1 A g^{-1}. It is clear that the NF cannot be charged and discharged, which fits well with the CV results. The GCD curves of $NiMoO_4$@$NiMoS_4$/NF-2 and $NiMoO_4$/NF deviate from the regular triangle, showing a deviation from linearity, which indicates that

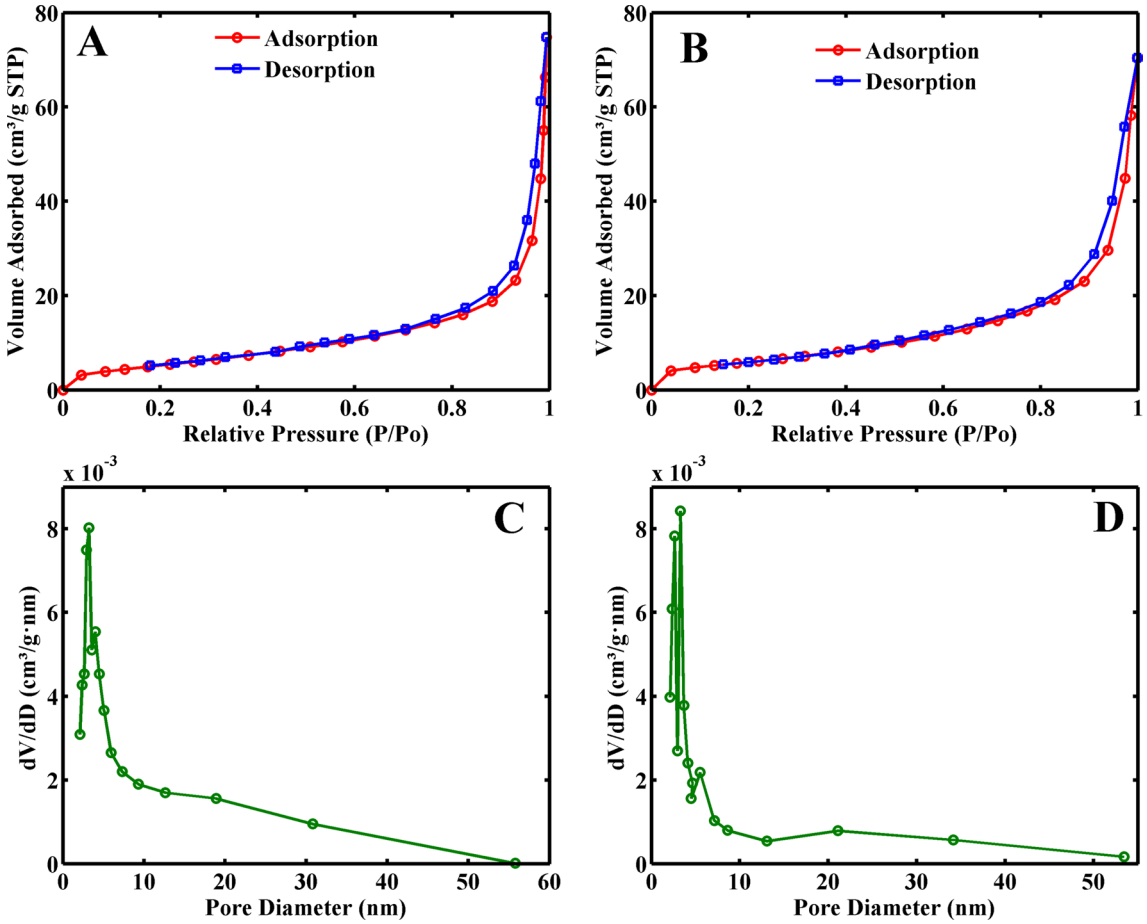

Fig. 5 Nitrogen adsorption–desorption isotherms of **A** $NiMoO_4$/NF and **B** $NiMoO_4$@$NiMoS_4$/NF-2; PSD of **C** $NiMoO_4$/NF and **D** $NiMoO_4$@$NiMoS_4$/NF-2

the $NiMoO_4$@$NiMoS_4$/NF-2 and $NiMoO_4$/NF are typical battery-type electrodes. According to the calculation, when the current density is 1 A g^{-1}, the C_p of $NiMoO_4$@$NiMoS_4$/NF-2 and $NiMoO_4$/NF is 1996 and 279 C g^{-1}, respectively. Compared with $NiMoO_4$/NF, the C_p of $NiMoO_4$@$NiMoS_4$/NF-2 increased by 7 times. These could be explained that O element is gradually replaced by S element with low electronegativity, which generates a more flexible core–shell structure to effectively prevent the disintegration of the structure and facilitate the transfer of electrons inside the materials. So, $NiMoS_4$@$NiMoO_4$/NF nanocomposite with core–shell structure possesses a larger surface area and more electrochemical active sites to facilitate the ion/electron transfer between the electrolyte and electrode materials. Figure 6C shows the C_p values of the $NiMoO_4$@$NiMoS_4$/NF-2 and $NiMoO_4$/NF at different current densities. When the current density is 1, 2, 4, 6, 8, 10, 15, 20, 25 and 30 A g^{-1}, the C_p of $NiMoO_4$/NF is 279, 249.8, 220.4, 204.6, 188.0, 171.0, 141.0, 106.0, 75.0 and 42.0 C g^{-1}, respectively, and the C_p of $NiMoO_4$@$NiMoS_4$/NF-2 is 1996.0, 1748.0, 1603.6, 1482.6, 1394.4, 1338.0, 1207.5, 1124.0, 1067.5 and 945.0 C g^{-1}, respectively.

In order to further understand the electrochemical properties of the electrode materials, the Faraday resistance for the $NiMoO_4$@$NiMoS_4$/NF-2 and $NiMoO_4$/NF was compared using EIS (Fig. 6D). The arc in a high frequency is usually related to the charge-transfer resistance (R_{ct}). In general, the smaller the radius of the arc, the faster the rate of charge transfer. From Fig. 6D, the R_{ct} values of $NiMoO_4$@$NiMoS_4$/NF-2 and $NiMoO_4$/NF are calculated to be 0.51 and 4.80 Ω, and the R_{ct} of $NiMoO_4$@$NiMoS_4$/NF-2 is far less than that of $NiMoO_4$/NF, indicating that $NiMoO_4$@$NiMoS_4$/NF-2 has a fast charge transfer rate and a fast redox reaction, which attributes to the transport and transfer between the electrolyte and electrode materials caused by highly conductive $NiMoO_4$@$NiMoS_4$ core–shell structure (M.J. Gao et al. 2019).

The effects of different concentrations of S^{2-} on the C_p of $NiMoO_4$@$NiMoS_4$/NF were investigated. When the concentrations of S^{2-} are 5 mM, 10 mM and 15 mM, the $NiMoO_4$@

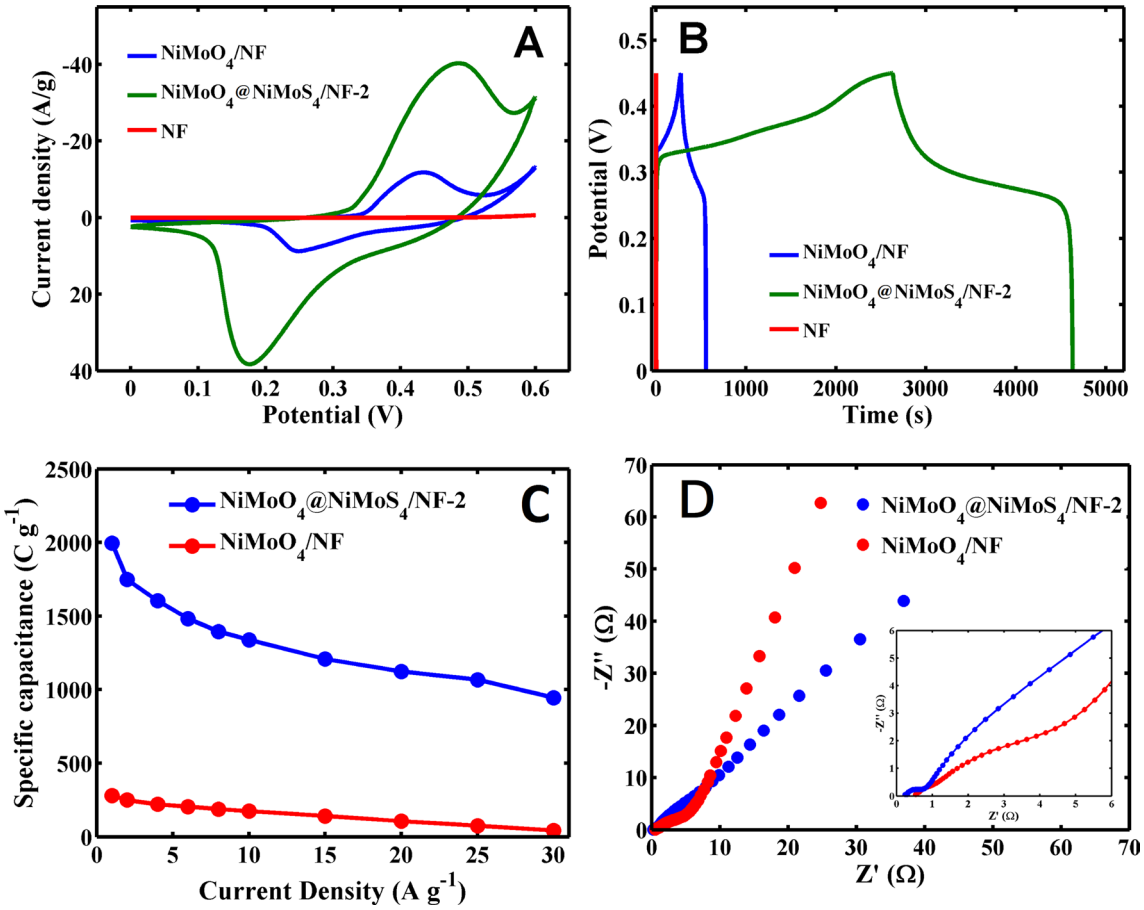

Fig. 6 **A** CVs of NF, $NiMoO_4$@$NiMoS_4$ and $NiMoO_4$ at 5 mV s^{-1}; **B** GCDs of NF, $NiMoO_4$@$NiMoS_4$ and $NiMoO_4$ at a current density of 1 A g^{-1}; **C** the corresponding specific capacity values at different current densities for $NiMoO_4$@$NiMoS_4$ and $NiMoO_4$; **D** Nyquist plots of $NiMoO_4$@$NiMoS_4$ and $NiMoO_4$ at open-circuit potential

$NiMoS_4$/NF electrode materials were marked as $NiMoO_4$@$NiMoS_4$/NF-1, $NiMoO_4$@$NiMoS_4$/NF-2 and $NiMoO_4$@$NiMoS_4$/NF-3, respectively. Figure 7A shows the CVs of $NiMoO_4$@$NiMoS_4$/NF-1, $NiMoO_4$@$NiMoS_4$/NF-2 and $NiMoO_4$@$NiMoS_4$/NF-3. It is very obvious that the enclosed area of $NiMoO_4$@$NiMoS_4$/NF-2 is larger than those of $NiMoO_4$@$NiMoS_4$/NF-1 and $NiMoO_4$@$NiMoS_4$/NF-3, indicating that the $NiMoO_4$@$NiMoS_4$/NF-2 has the largest C_p. Figure 7B shows the GCDs of $NiMoO_4$@$NiMoS_4$/NF-1, $NiMoO_4$@$NiMoS_4$/NF-2 and $NiMoO_4$@$NiMoS_4$/NF-3. By calculation, when the current density is 1 A g^{-1}, the C_p of $NiMoO_4$@$NiMoS_4$/NF-1, $NiMoO_4$@$NiMoS_4$/NF-2 and $NiMoO_4$@$NiMoS_4$/NF-3 is 465.1, 1996.0 and 1311.0 C g^{-1}, respectively. Moreover, the C_p of $NiMoO_4$@$NiMoS_4$/NF-1, $NiMoO_4$@$NiMoS_4$/NF-2 and $NiMoO_4$@$NiMoS_4$/NF-3 at different current densities is shown in Fig. 7C. When the current density is 1, 2, 4, 6, 8, 10, 15, 20, 25 and 30 A g^{-1}, the specific capacity of $NiMoO_4$@$NiMoS_4$/NF-1 is 465.1, 436.6, 398.0, 361.2, 340.8, 319.0, 262.5, 212.0, 152.5 and 96.0 C g^{-1}, respectively, and the specific capacity of $NiMoS_4$/NF-3 is 1311.0, 1169.6, 1047.2, 978.6, 915.2, 852.0, 775.4, 704.0, 650.0 and 633.0 C g^{-1}, respectively. Figure 8 is SEM images of $NiMoO_4$@$NiMoS_4$/NF-1 (A), $NiMoO_4$@$NiMoS_4$/NF-2 (B) and $NiMoO_4$@ $NiMoS_4$/NF-3 (C). According to Fig. 8A, a large number of loose laminated structures ($NiMoS_4$) are observed after the partial O element in the $NiMoO_4$@$NiMoS_4$ composite was indeed replaced by the S element. With the increasing concentration of $(NH_4)_2S$, $NiMoS_4$ nanosheets get denser and denser (Fig. 8B). However, when the S^{2-} concentration further increases, too many sheet structures give rise to serious agglomeration on the surface of the samples (Fig. 8C), which results in a decline in effective active area and active sites of the electrode materials (Lv et al. 2022). Therefore, when the S^{2-} concentration is suitable, the $NiMoO_4$@$NiMoS_4$/NF electrode material will show a better electrochemical performance. Table 1 compares the value of C_p and cycling stability for the $NiMoO_4$@$NiMoS_4$/NF with those of some other Ni and Mo bimetallic oxide and sulfide electrode materials for SCs reported in the previous literatures. The results showed that the C_p of

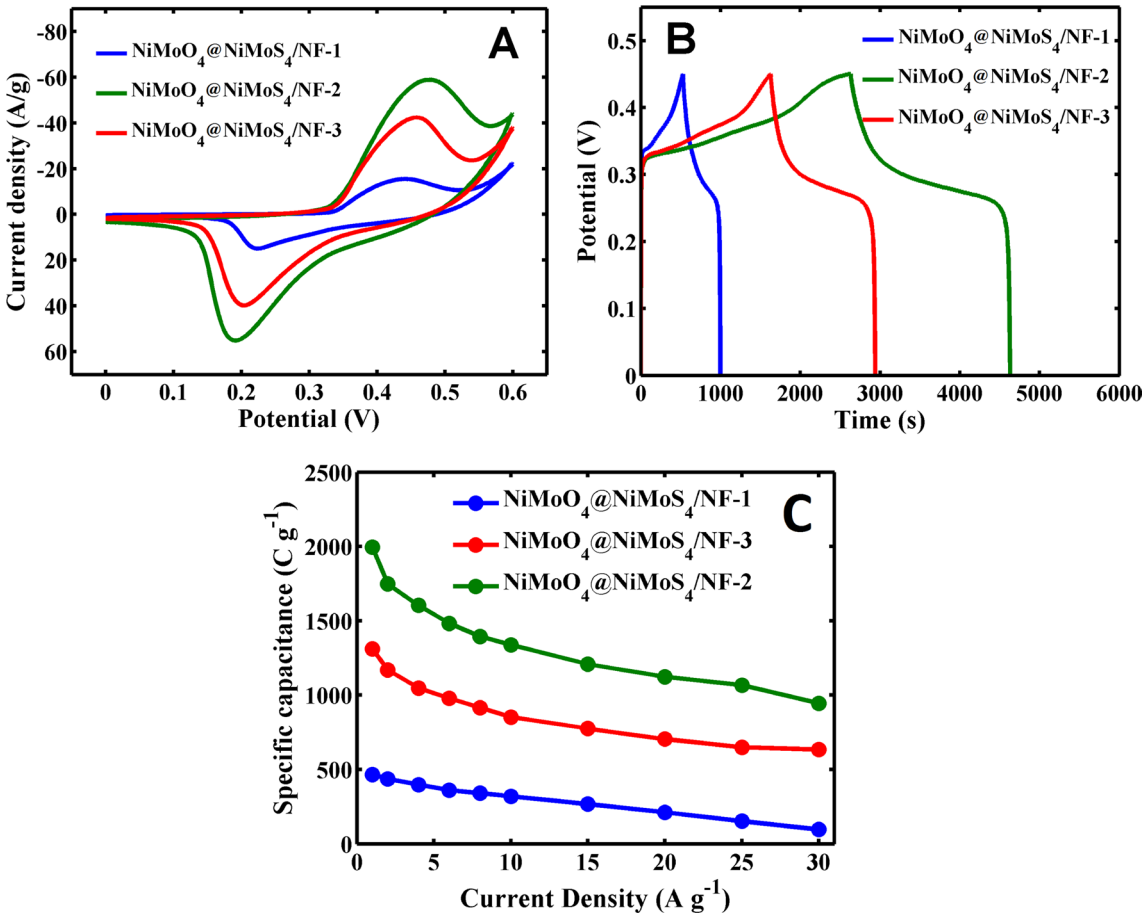

Fig. 7 **A** CVs of $NiMoO_4$@$NiMoS_4$/NF-1, $NiMoO_4$@$NiMoS_4$/NF-2 and $NiMoO_4$@$NiMoS_4$/NF-3 at a scan rate of 5 mV s^{-1} **B** GCDs of $NiMoO_4$@$NiMoS_4$/NF-1, $NiMoO_4$@$NiMoS_4$/NF-2 and $NiMoO_4$@$NiMoS_4$/NF-3 at a current density of 0.5 A g^{-1}, **C** the corresponding specific capacity values at different current densities for $NiMoO_4$@$NiMoS_4$/NF-1, $NiMoO_4$@$NiMoS_4$/NF-2 and $NiMoO_4$@$NiMoS_4$/NF-3

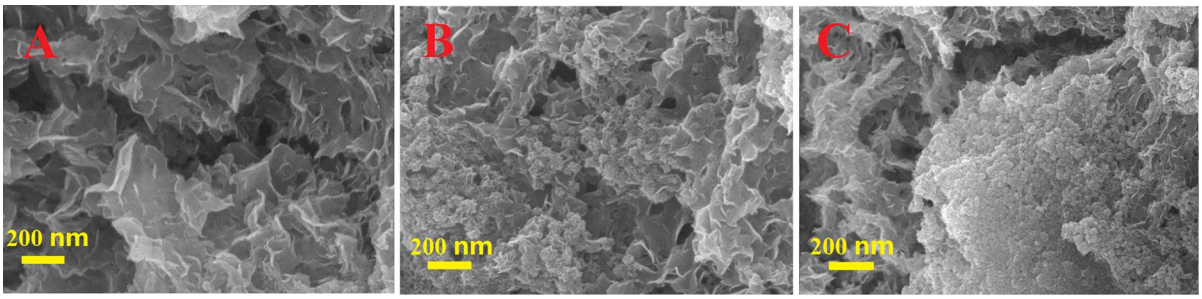

Fig. 8 SEM images of $NiMoO_4$@$NiMoS_4$/NF-1 **A**, $NiMoO_4$@$NiMoS_4$/NF-2 **B** and $NiMoO_4$@ $NiMoS_4$/NF-3 **C**

the $NiMoO_4$@$NiMoS_4$/NF-2 is higher than those of similar materials, which may be related to the good electrical conductivity of the materials.

In Fig. 9A, the CV curves of $NiMoO_4$@$NiMoS_4$/NF-2 at different scanning speeds are investigated. With the increase of scanning rates, the oxidation and reduction peaks shift to the high and low potential (Tang et al. 2020), respectively. At different scanning rates, the CVs in shape are similar, showing excellent redox reversibility. In Figs. 9B and 9C, the GCDs of $NiMoO_4$@$NiMoS_4$/NF-2 at different current densities are investigated. With the increase of current density, the charging and discharging times decrease, which

Table 1 Comparison of C_p and cycling stability for the $NiMoO_4$@$NiMoS_4$/NF with reported Ni and Mo bimetallic oxide and sulfide electrode materials for SCs

Electrode materials	C_p	Cycling stability	Refs.
$NiMoS_4$-A	313 C g^{-1} (1 A g^{-1})	10,000 cycles 82% (5 A g^{-1})	Du et al. (2017)
1D-$NiMoO_4$@2D-$NiMoS_4$	457.7 C g^{-1} (5 A g^{-1})	1000 cycles 81.4% (10 A g^{-1})	Gao et al. (2019)
$NiMoO_4$	546 C g^{-1} (1 A g^{-1})	2000 cycles 88% (20 A g^{-1})	Murugan et al. (2021)
$NiMoO_4$/rGO	700 C g^{-1} (1 A g^{-1})	2000 cycles 91% (20 A g^{-1})	Murugan et al. (2021)
$NiMoS_4$–rGO	500 C g^{-1} (1 A g^{-1})	5000 cycles 96.05% (8 A g^{-1})	Wei et al. (2019)
$Co(OH)_2$@$NiMoS_4$	1047 C g^{-1} (1 A g^{-1})	2000 cycles 84% (10 A g^{-1})	Li et al. (2020a, b)
$NiMoO_4$@$NiMoS_4$/NF	1996 C g^{-1} (1 A g^{-1})	5000 cycles 83.1% (20 A g^{-1})	This work

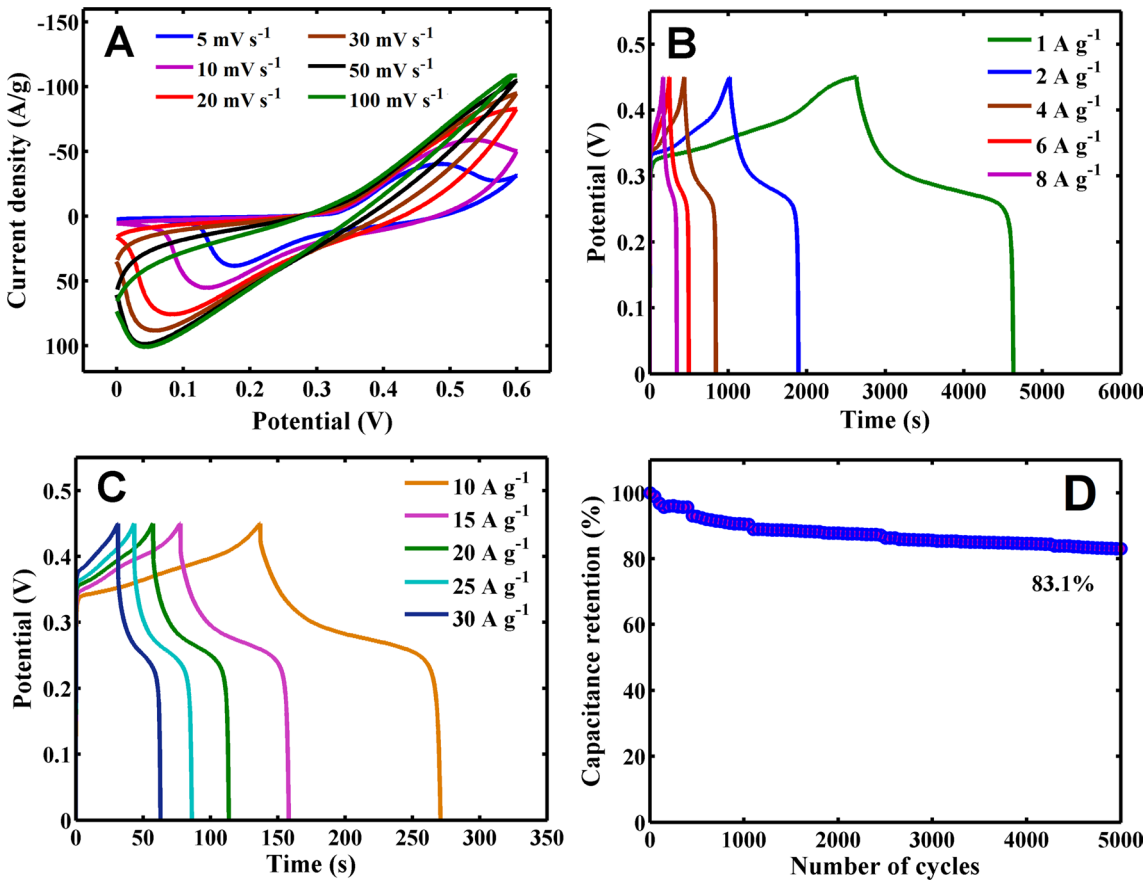

Fig. 9 (**A**) CVs of $NiMoO_4$@$NiMoS_4$/NF-2 at different scan rates; (**B** and **C**) GCDs of $NiMoO_4$@$NiMoS_4$/NF-2 at different current densities; (**D**) cyclic stability of $NiMoO_4$@$NiMoS_4$/NF-2 at a current density of 20 A g^{-1}

is attributed to the fact that the ion diffusion is difficult in the electrolyte and the charge transfer at electrode materials is slow at high current density. The cyclic stability of $NiMoO_4$@$NiMoS_4$/NF-2 at a current density of 20 A g^{-1} is shown in Fig. 9D, and the results show that the capacity retention rate of $NiMoO_4$@$NiMoS_4$/NF-2 reaches 83.1% after 5000 cycles. At the beginning, the C_p decays rapidly, and at the later stage, the C_p is relatively stable. This may be because it is difficult for ions/electrons to enter the electrode material inside at a higher current density, thus causing the C_p to decline.

In a two-electrode system, the hybrid SC—$NiMoO_4$@$NiMoS_4$/NF-2//AC was constructed with $NiMoO_4$@$NiMoS_4$/NF as the positive electrode and AC as the negative electrode in 1 M KOH electrolyte. Combined with the voltage window of 0–0.45 V for $NiMoO_4$@$NiMoS_4$/NF-2, the voltage window of − 1.0–0 V for AC and the maximum polarization effect of the application window, the voltage window of the $NiMoO_4$@$NiMoS_4$/NF-2//AC asymmetric SC is extended to 0 to 1.45 V (X.Y. Xu et al. 2020). The electrochemical tests of $NiMoO_4$@$NiMoS_4$/NF-2//AC at different scanning rates and current densities are shown in

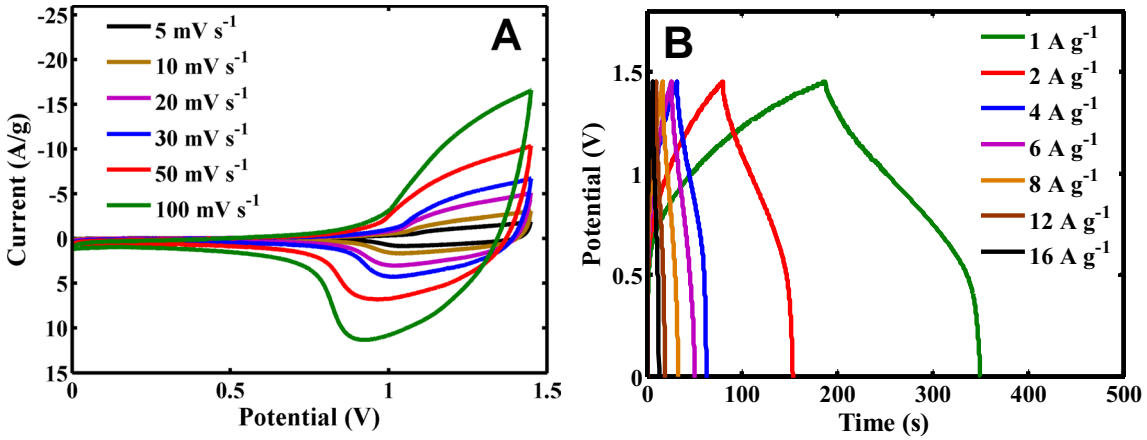

Fig. 10 **A** CVs of $NiMoO_4$@$NiMoS_4$/NF-2//AC at different scan rates (5, 10, 20, 30, 50 and 100 mV s^{-1}); **B** GCDs of $NiMoO_4$@$NiMoS_4$/NF-2/AC at different current densities (1, 2, 4, 6, 8, 12 and 16 A g^{-1})

Fig. 10. It can be clearly seen from Fig. 10 that the curve of electrode material presents non-rectangular CV curve (Fig. 10A) and nonlinear GCD curve (Fig. 10B), which shows that the C_p value is mainly attributed to Faraday redox reaction. When the current density is 1, 2, 4, 6, 8, 12 and 16 A g^{-1}, the C_p value is 162.6, 147.8, 122.4, 144.6, 128.8, 112.8 and 100.8 C g^{-1}, respectively. At high current density, the C_p of the device is gradually reduced due to the inherent resistance in the electrode and the lack and loss of Faraday reaction for electrode materials. Moreover, the energy density and power density are calculated to be 32.75 Wh kg^{-1} and 725.09 W kg^{-1}, respectively.

Conclusions

In conclusion, a novel $NiMoO_4$@$NiMoS_4$ core–shell nanocomposite is facilely grown on NF *via* hydrothermal reaction and high-temperature calcination methods. The $NiMoO_4$@$NiMoS_4$/NF-2 shows ultra-high C_p and good cycle stability, and these could be mainly explained that the typical core–shell structure possesses a larger active surface area and abundant electrochemical active sites, which is conducive to maximize the utilization of the active substance of $NiMoO_4$@$NiMoS_4$/NF-2 in energy storage. The nanosheet structure as the "shell" can promote the charge transfer from electrode material to the NF so as to realize the Faraday process quickly. At a current density of 1 A g^{-1}, the C_p value of the $NiMoO_4$@$NiMoS_4$/NF-2 reaches 1996.0 C g^{-1}, which is much higher than the C_p values of similar materials reported in the literature. So, the $NiMoO_4$@$NiMoS_4$/NF is an outstanding electrode material for hybrid SCs.

Acknowledgements The authors gratefully acknowledge the financial support of this study by the National Natural Science Foundation of China (NSFC-31860468).

Declarations

Conflict of interest The authors declare that they have no known competing financial interests or personal relationships that could have appeared to influence the work reported in this paper.

References

Ates M, Yildirim M (2020) The synthesis of rGO/RuO_2, rGO/PANI, RuO_2/PANI and RGO/RuO_2/PANI nanocomposites and their supercapacitors. Polym Bull 77:2285–2307

Azad M, Hussain Z, Baig MM (2020) MWCNTs/NiS_2 decorated Ni foam based electrode for high-performance supercapacitors. Electrochim Acta 345:136196

Banda H, Dou JH, Chen TY, Libretto NJ, Chaudhary M, Bernard GM, Miller JT, Michaelis VK, Dinca M (2021) High-capacitance pseudocapacitors from Li^+ ion intercalation in nonporous, electrically conductive 2D coordination polymers. J Am Chem Soc 143:2285–2292

Boota M, Gogotsi Y (2019) MXene-conducting polymer asymmetric pseudocapacitors. Adv Energy Mater 9:1802917

Chen D, Jiang K, Huang TT, Shen GZ (2020) Recent advances in fiber supercapacitors: materials, device configurations, and applications. Adv Mater 32:1901806

Cho SI, Lee SB (2008) Fast electrochemistry of conductive polymer nanotubes: synthesis, mechanism, and application. Acc Chem Res 41:699–707

Choi NS, Chen ZH, Freunberger SA, Ji XL, Sun YK, Amine K, Yushin G, Nazar LF, Cho J, Bruce PG (2012) Challenges facing lithium batteries and electrical double-layer capacitors. Angew Chem Int Ed 51:9994–10024

Du DW, Lan R, Humphreys J, Xu W, Xie K, Wang HT, Tao SW (2017) Synthesis of $NiMoS_4$ for high-performance hybrid supercapacitors. J Electrochem Soc 164:2881–2888

Fleischmann S, Leistenschneider D, Lemkova V, Kruner B, Zeiger M, Borchardt L, Presser V (2017) Tailored mesoporous carbon/

vanadium pentoxide hybrid electrodes for high power pseudocapacitive lithium and sodium intercalation. Chem Mater 29:8653–8662

Gao MJ, Le K, Xu DM, Wang Z, Wang FL, Liu W, Yu HJ, Liu JR, Chen CZ (2019) Controlled sulfidation towards achieving core-shell 1D-$NiMoO_4$@2D-$NiMoS_4$ architecture for high-performance asymmetric supercapacitor. J Alloys Compd 804:27–34

Guo SH, Feng Y, Qiu JH, Li XD, Yao JF (2019) Leaf-shaped bimetallic sulfides@N-doped porous carbon as advanced lithium-ion battery anode. J Alloy Compd 792:8–15

Jayachandiran J, Yesuraj J, Arivanandhan J, Muthuraaman B, Jayavel R, Nedumaran D (2021) Bifunctional investigation of ultrasmall SnO_2 nanoparticle decorated rGO for ozone sensing and supercapacitor applications. RSC Adv 11:856–866

Ji HX, Zhao X, Qiao ZH, Jung J, Zhu YW, Lu YL, Zhang LL, Marc-Donald AH, Ruoff RS (2014) Capacitance of carbon-based electrical double-layer capacitors. Nat Commun 5:3317

Kostoglou N, Koczwara C, Prehal C, Erziyska VT, Babic B, Matovic B, Constantinides G, Tampaxis C, Charalambopoulou G, Steriotis T, Hinder S, Hinder S, Baker M, Polychronopoulou K, Doumanidis C, Paris O, Mitterer C, Rebholz C (2018) Nanoporous activated carbon cloth as a versatile material for hydrogen adsorption, selective gas separation and electrochemical energy storage. Nano Energy 46:277–289

Krishnamoorthy K, Pazhamalai P, Kim S (2018) Two-dimensional siloxene nanosheets: novel high-performance supercapacitor electrode materials. Energy Environ Sci 11:1595–1602

Li XL, Zhi LJ (2018) Graphene hybridization for energy storage applications. Chem Soc Rev 47:3189–3216

Li JX, Zhao JW, Qin LR, Zhang QT, Tang XL, Xu YY (2020a) Hierarchical $Co(OH)_2$@$NiMoS_4$ nanocomposite on carbon cloth as electrode for high-performance asymmetric supercapacitors. RSC Adv 10:22606–22615

Li Y, Wei QL, Wang R, Zhao JK, Quan ZL, Zhan TR, Li DX, Xu J, Teng HN, Hou WG (2020b) 3D hierarchical porous nitrogen-doped carbon/Ni@NiO nanocomposites self-templated by cross-linked polyacrylamide gel for high performance supercapacitor electrode. J Colloid Interface Sci 570:286–299

Liu YH, Xu JL, Gao X, Sun YL, Lv JJ, Shen S, Chen LS, Wang SD (2017) Freestanding transparent metallic network based ultrathin, foldable and designable supercapacitors. Energy Environ Sci 10:2534–2543

Lv JM, Bai DX, Yang L, GuoY YH, Xu SL (2018) Bimetallic sulfide nanoparticles confined by dual-carbon nanostructures as anodes for lithium-/sodium-ion batteries. Chem Commun 54:8909–8912

Lv XR, Feng L, Lin XY, Ni YN (2022) A novel 3D $MnNi_2O_4$@$MnNi_2S_4$ core-shell nano array for ultra-high capacity electrode material for supercapacitors. J Energy Storage 47:103579

Mariyappan V, Keerthi M, Chen SM, Boopathy G (2020) Facile synthesis of alpha-Sm_2S_3/MoS_2 bimetallic sulfide as a high-performance electrochemical sensor for the detection of antineoplastic drug 5-fluorouracil in a biological samples. J Electrochem Soc 167:117506

MuruganE GS, Santhoshkumar S (2021) Hydrothermal synthesis, characterization and electrochemical behavior of $NiMoO_4$ nanoflower and $NiMoO_4$/rGO nanocomposite for high-performance supercapacitors. Electrochim Acta 392:138973

Najafpour MM, Holynska M, Salimi S (2015) Applications of the "nano to bulk" Mn oxides: Mn oxide as a swiss army knife. Coord Chem Rev 285:65–75

Priyadharsini CI, Marimuthu G, Pazhanivel T, Anbarasan PM, Aroulmoji V, Siva V, Mohana L (2020) Sol-gel synthesis of Co_3O_4 nanoparticles as an electrode material for supercapacitor applications. J Sol-Gel Sci Technol 96:416–422

Salunkhe RR, Kaneti YV, Kim J, Kim JH, Yamauchi Y (2016) Nanoarchitectures for metal-organic framework-derived nanoporous carbons toward supercapacitor applications. Acc Chem Res 49:2796–2806

Sathiya M, Prakash AS, Ramesha K, Tarascon JM, Shukla AK (2011) V_2O_5-anchored carbon nanotubes for enhanced electrochemical energy storage. J Am Chem Soc 133:16291–16299

Savjani N, Lewis EA, Bissett MA, Brent JR, Dryfe RAW, Haigh SJ, Brien PO (2016) Synthesis of lateral size-controlled monolayer 1H-MoS_2@oleylamine as supercapacitor electrodes. Chem Mater 28:657–664

Shao YL, El-Kady MF, Wang LJ, Zhang QH, Li YG, Wang HZ, Mousavi MF, Kaner RB (2015) Graphene-based materials for flexible supercapacitors. Chem Soc Rev 4:3639–3665

Shrestha KR, Kandula S, Kim NH, Lee JH (2021) Core cation tuned $MxCo_{3-x}S_4$@$NiMoS_4$ [M = Ni, Mn, Zn] core-shell nanomaterials as advanced all solid-state asymmetric supercapacitor electrode. Chem Eng J 405:127046

Shrivastav V, Sundriyal S, Goel P, Shrivastav V, Tiwari UK, Deep A (2020) ZIF-67 derived Co_3S_4 hollow microspheres and WS_2 nanorods as a hybrid electrode material for flexible 2V solid-state supercapacitor. Electrochim Acta 345:136194

Tang DM, Zhao RF, Xie J, Zhou KH, Han Y, Wu XY, Wu HY, Diao GW, Chen M (2020) Bimetallic sulfide Co_8FeS_8/N-C dodecahedral nanocages via cation exchange as counter electrode for dye-sensitized solar cells. J Alloy Compd 829:s

TaoK HX, Cheng QH, Yang YJ, Yang Z, Ma QX (2018) A Zinc sobalt sulfide nanosheet array derived from a 2D bimetallic metal-organic frameworks for high-performance supercapacitors. Chem-Eur J 24:12584–12591

Wang KB, Wang SE, Liu JD, Guo YX, Mao FF, Wu H, Zhang QC (2021) Fe-Based Coordination polymers as battery-type electrodes in semi-solid-state battery-supercapacitor hybrid devices. ACS Appl Mater Interfaces 13:15315–15323

Wei M, Wu X, Yao Y, Yu S, Sun R, Wong CP (2019) Toward high micro-supercapacitive performance by constructing graphene-supported $NiMoS_4$ hybrid materials on 3D current collectors. ACS Sustain Chem Eng 7:19779–19786

Xu YX, Shi GQ, Duan XF (2015) Self-assembled three-dimensional graphene macrostructures: synthesis and applications in supercapacitors. Acc Chem Res 48:1666–1675

Xu XY, Liang L, Liu QQ, Zhang XJ, Zhao Y, Qiao SL (2020) In-situ induced sponge-like $NiMoS_4$ nanosheets on self-supported nickel foam skeleton for electrochemical capacitor electrode. Colloids Surf A 602:125099

Yang P, Wang S, Hu J, Sun XF, Shi JJ, Xing HL (2020) Facile electrochemical deposition of porous $NiCo_2S_4$ on $FeCo_2O_4$ array as a positive material for battery-supercapacitor hybrid device. J Electrochem Soc 167:160554

Yu HY, Qian C, Ren HJ, Chen M, Tang DM, Wu HY, Lv RG (2020) Enhanced catalytic properties of bimetallic sulfides with the assistance of graphene oxide for accelerating triiodide reduction in dye-sensitized solar cells. Sol Energy 207:1037–1044

Zhai MM, ChengY JinY, Hu JB (2019) Solvothermal synthesis of flower-like structure Cu-Mn bimetallic sulfide on Ni-foam for high-performance symmetric supercapacitors. Int J Hydrog Energy 44:13456–13465

Zhai SL, Karahan HE, Wang CJ, Pei ZX, Wei L, Chen Y (2020) 1D supercapacitors for emerging electronics: current status and future directions. Adv Mater 32:1902387

Zhao Y, Cao JY, Zhang Y, Peng HS (2020) Gradually crosslinking carbon nanotube array in mimicking the beak of giant squid for compression-sensing supercapacitor. Adv Funct Mater 30:1902971

Zhao J, Cheng H, Zhang ZH, Liu Y, Song JN, Liu T, He YN, Meng AL, Sun CL, Hu MM, Wang L, Li GC, Huang JF, Li ZJ (2022)

The semicoherent interface and vacancy engineering for constructing Ni(Co)Se_2@Co(Ni)Se_2 heterojunction as ultrahigh-rate battery-type supercapacitor cathode. Adv Funct Mater 32:2202063